The Astrophysical Journal, 654:650–664, 2007 January 1

OBSERVATIONS SUPPORTING THE ROLE OF MAGNETOCONVECTION IN ENERGY SUPPLY TO THE QUIESCENT SOLAR ATMOSPHERE

Scott W. McIntosh, Alisdair R. Davey, and Donald M. Hassler
Department of Space Studies, Southwest Research Institute, Boulder, CO

James D. Armstrong
Institute for Astronomy, University of Hawaii, Kula, HI

Werner Curdt and Klaus Wilhelm
Max Planck Institute for Solar System Research, Katlenburg-Lindau, Germany

and

Gang Lin
Department of Electrical, Computer, and Systems Engineering, Rensselaer Polytechnic Institute, Troy, NY
Received 2006 July 8; accepted 2006 September 7

ABSTRACT

Identifying the two physical mechanisms behind the production and sustenance of the quiescent solar corona and solar wind poses two of the outstanding problems in solar physics today. We present analysis of spectroscopic observations from the *Solar and Heliospheric Observatory* that are consistent with a single physical mechanism being responsible for a significant portion of the heat supplied to the lower solar corona and the initial acceleration of the solar wind; the ubiquitous action of magnetoconvection-driven reprocessing and exchange reconnection of the Sun's magnetic field on the supergranular scale. We deduce that while the net magnetic flux on the scale of a supergranule controls the injection rate of mass and energy into the transition region plasma, it is the global magnetic topology of the plasma that dictates whether the released ejecta provides thermal input to the quiet solar corona or becomes a tributary that feeds the solar wind.

Subject headings: solar wind — Sun: corona — Sun: granulation — Sun: magnetic fields — Sun: transition region — Sun: UV radiation

Online material: color figures

1. INTRODUCTION

The relentless, convection-driven reprocessing of magnetic fields on the Sun has been dubbed the "magnetic carpet" (e.g., Schrijver et al. 1997; Hagenaar et al. 1997, 1999; Title & Schrijver 1998). Detailed observations of the Sun's photospheric magnetic field have been used to deduce that the turbulent motion of the ionized gas in the solar interior causes small bipolar magnetic flux elements to be carried toward the photosphere. There, through their annihilation, they contribute the global magnetic structure of the outer solar atmosphere and are a source of energy to the corona and solar wind (Schrijver et al. 1998; Priest & Schrijver 1999; Priest et al. 2002).

Numerical simulations of magnetoconvection (Cattaneo et al. 2003) and tectonic models of the magnetic carpet (Priest et al. 2002) show that the emerging bipolar elements are advected toward the boundaries of large convective cells with typical diameters of 15–35 Mm (e.g., Hagenaar et al. 1997). These large supergranular convection cells are relatively easy to observe in the solar photosphere and chromosphere, and comprise the "chromospheric network." Over periods of many hours to days, the constant convective dredging of the magnetic field imposes a net magnetic polarity on a supergranule. This determines the polarity of the emerging magnetic dipoles, which are annihilated through magnetic reconnection (e.g., Parker 1988, 1994; Priest & Forbes 2000). It has been postulated that energy stored in, and eventually released by, these small annihilated magnetic dipoles is the simplest and most efficient means of providing the 100 W m^{-2} required to produce the Sun's ambient 2×10^6 K corona (Priest & Schrijver 1999; Priest et al. 2002; Parker 1994) and to load and accelerate mass into the solar wind (Priest & Forbes 2000; Wang 1998; Wang & Sheeley 2004).

Recently, observations from the Solar Ultraviolet Measurement of Emitted Radiation (SUMER; Wilhelm et al. 1995), the Extreme-Ultraviolet Imaging Telescope (EIT; Delaboudinière et al. 1995), and the Michelson Doppler Imager (MDI; Scherrer et al. 1995), instruments on board the *Solar and Heliospheric Observatory* (*SOHO*; Fleck et al. 1995), have provided insight into the origins of the fast solar wind in coronal holes (Hassler et al. 1999; Dammasch et al. 1999; Xia et al. 2003, 2004; Tu et al. 2005a, 2005b). SUMER "spectroheliogram," or raster, observations were employed to quantitatively examine the origins of the solar wind by correlating Doppler velocity measurements of Ne viii (formed at about 600,000 K in the upper solar transition region; Mazzotta et al. 1998) to a proxy for the gross supergranulation pattern of chromospheric network structure: bright Si ii emission (formed at about 10,000 K).

Results of these prior studies suggested a clear correlation between the observed Ne viii blueshift[1] and the chromospheric network pattern seen in Si ii. We show that while there is indeed a strong correlation between bright Si ii emission and Ne viii blue Doppler shifts, it is limited to regions that occur at the intersections of three or more supergranules (see, e.g., Fig. 3). We call these locations "bright network vertices."

[1] In this paper we use the convention that a blueshift is associated with a negative velocity, and as such a blue Doppler shift indicates the presence of plasma moving toward the observer, possibly indicating an outflow from the Sun.

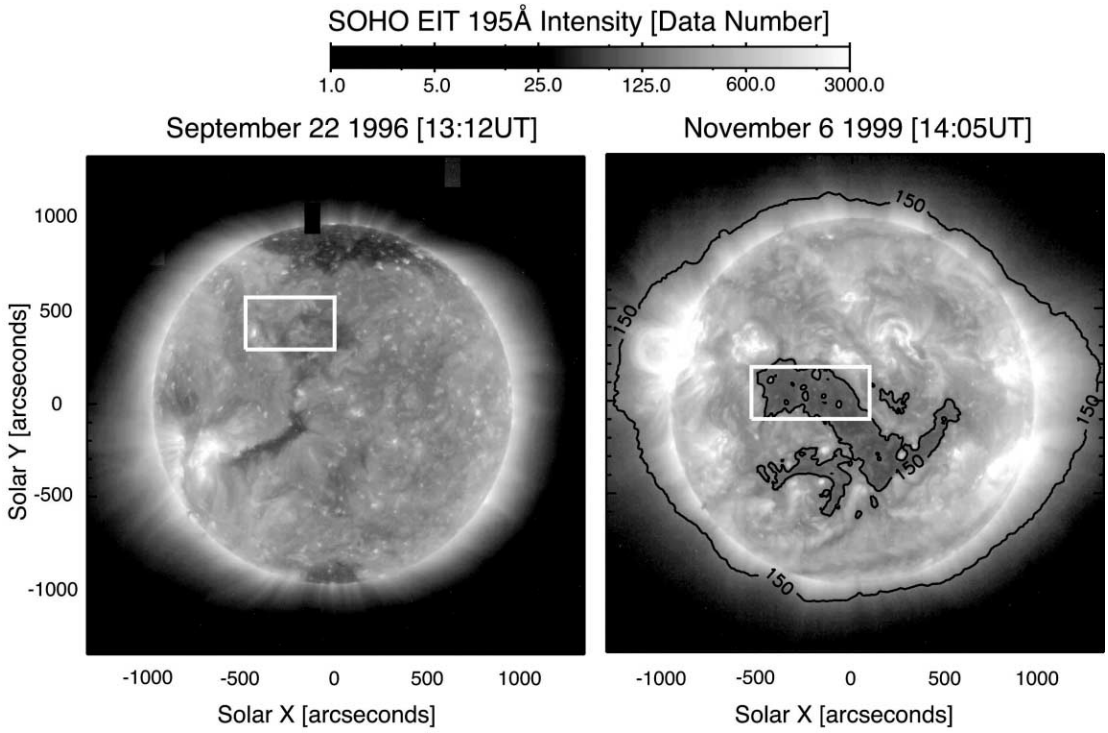

FIG. 1.—*SOHO* EIT images of the Sun's corona (seen in 1.5 MK, Fe XII 195 Å) on 1996 September 22 (*left*) and 1999 November 6 (*right*). The right panel shows the outline of the equatorial coronal hole region studied in this paper as a black closed contour (at the 150 DN level). Also shown are the regions of the solar atmosphere concurrently mapped by the SUMER instrument (*white outlined rectangles*) on both days. [*See the electronic edition of the Journal for a color version of this figure.*]

We demonstrate that a substantial fraction of the blueshifted Ne VIII plasma in coronal holes is not correlated with the bright Si II emission that forms the supergranular boundaries or bright network vertices, consistent with the recent analysis of Aiouaz et al. (2005). We investigate the remaining portion of the blueshifted Ne VIII plasma in the coronal hole to examine the mechanism behind the energetic processes taking place in the outer solar atmosphere.

We find that a critical—and largely overlooked—step toward understanding the excess Ne VIII Doppler shift lies in the interpretation of the C IV emission line, formed in the transition region at roughly 100,000 K between Si II and Ne VIII. Data available at this thermodynamic midpoint allow us to physically couple the spatial variation of the lower temperature Si II and higher temperature Ne VIII plasmas to form an entirely new interpretation of these well-studied data.

We present the self-consistent analysis, comparison, and interpretation of the results derived from spectroscopic observations of coronal hole and quiet-Sun regions, which point to the magnetic carpet's constant recycling of magnetic flux as a significant energy supply mechanism to the outer solar atmosphere. Indeed, we deduce that the difference in the form of the energy provided to the plasma stems, rather simply, from whether or not its magnetic topology is "open" (coronal hole, largely kinetic) or "closed" (quiet Sun, largely thermal) to interplanetary space.

2. OBSERVATIONS AND DATA REDUCTION

Many investigations into SUMER raster observations of coronal holes have focused on the Sun's polar regions (Hassler et al. 1999; Dammasch et al. 1999; Xia et al. 2003; Tu et al. 2005a). We instead concentrate on an equatorial coronal hole (hereafter referred to as a coronal hole) to minimize interpretative error and any line-of-sight effects on the magnetic fields and Doppler images. Viewing an equatorial region largely removes the need to perform latitude-dependent transforms to the data. Indeed, such transforms to the Doppler data are not simple and require a significant amount of a priori information of the magnetic structures present because the plasma and its observed flows are intimately bound to those structures.

We use two SUMER rasters in the 1530–1555 Å spectral range. This portion of the solar UV spectrum contains emission lines of singly ionized silicon (Si II) with a rest wavelength of 1533.43 Å, seven times ionized neon (Ne VIII) at 1540.84 Å (in second spectral order), and two lines of three times ionized carbon (C IV) at 1548.20 and 1550.77 Å. The two C IV lines behave identically, and so we only consider information from the former in this paper, as it has a better signal-to-noise ratio. These three emission lines span the highly dynamic solar transition region; the thermodynamic region of the solar atmosphere coupling the chromosphere at 10,000 K to the upper transition region or low solar corona at nearly 1×10^6 K.

Each SUMER raster that we have studied uses detector A, the $1'' \times 300''$ slit (SUMER slit 2), exposure times of 150 s, and a $3''$ raster step size from west to east in direction. The first raster is of a coronal hole, from 1999 November 6 (14:00–00:00 UT), and the second is of a well-studied (Hassler et al. 1999; Dammasch et al. 1999; Xia et al. 2004; Tu et al. 2005b) portion of quiet Sun from 1996 September 22 (00:40–08:28 UT). The EIT 195 Å reference images (presented in Fig. 1) provide contextual data on the hot solar corona (emission of 11 times ionized iron, Fe XII, at about 1.5×10^6 K; Delaboudinière et al. 1995) nearest to the start of each observation along with the rectangular region rastered by SUMER. Similarly, we use the full-disk photospheric MDI line-of-sight magnetograms nearest to the start of each observation to explore the magnetic environment in SUMER's field of view.

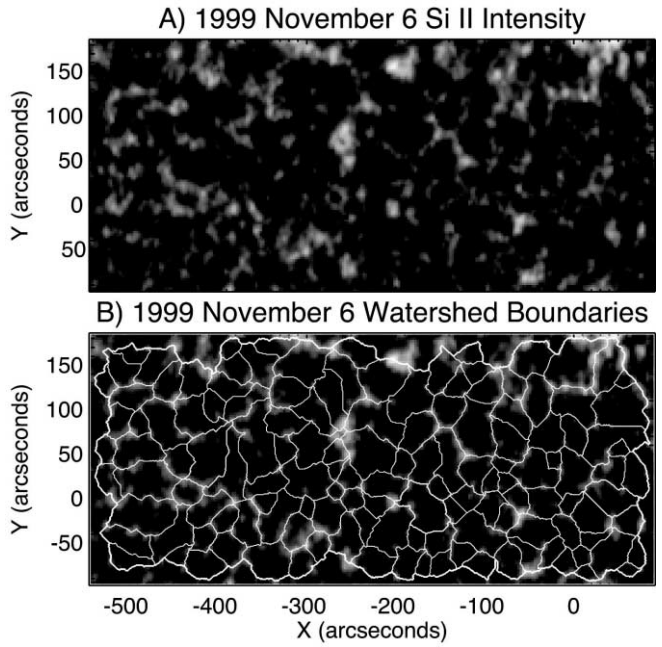

FIG. 2.—Comparison of the 1999 November 6 Si II intensity raster and the numerically determined watershed segmentation boundaries that we use throughout as a proxy for the underlying supergranular network cell pattern. Note that for the bulk of the statistics presented later, we use a version of the boundaries that is artificially thickened to 3 pixels (adding 1 pixel to either side of the boundary), giving them an assumed (artificial) thickness of 9″. [*See the electronic edition of the Journal for a color version of this figure.*]

The robust absolute wavelength calibration of the observed line spectra in SUMER raster observations is critical for attempts to accurately measure and isolate the source regions of the fast solar wind. Davey et al. (2006) quantified the small (persistent) electronic imperfections of SUMER detector A and developed an improved method to correct for the systematic shifting of the resulting solar UV spectra when acquired in raster mode. While the detector imperfections are small in pixel terms (± 0.5 pixels), in terms of velocity, at 1535 Å these translate to ± 4 km s^{-1} (Wilhelm et al. 1995). At this magnitude they influence any attempt at absolute physical interpretation of the data.

By mapping the locations of 10 laboratory measured emission lines of neutral silicon (Si I) in the 1530–1555 Å range at each spatial row of pixels, Davey et al. (2006) performed a self-consistent wavelength calibration for nine SUMER detector A raster observations, including the two discussed above. The result of this calibration is a set of Doppler velocities in the principal science lines (Si II, C IV, and Ne VIII) to an accuracy of about ± 1 km s^{-1}. The corrected data form the "cleanest" set of SUMER raster observations available, and their contents have prompted the investigation presented here.

We note that, following the instrumental discussion of Davey et al. (2006; § 4) and the topological argument in McIntosh et al. (2006; § 3), we use 770.420 Å as the rest wavelength of the Ne VIII emission line to compute the Doppler velocity maps presented in this paper. This choice agrees with one of the laboratory determinations of the rest wavelength for this emission line (Fawcett et al. 1961) and will be the subject of a future publication (A. R. Davey & S. W. McIntosh 2006, in preparation).

2.1. *Supergranular Boundaries*

In Figure 2*a*, we show the empirically determined supergranular boundaries derived from the Si II intensity image, using an enhanced watershed segmentation technique (Lin et al. 2003). Watershed segmentation uses the derivative of the intensity image as a topographic map to determine numerical "watershed basins." The places where the watershed basins meet form an initial watershed boundary in regard to which a model-based object merging is used to eliminate oversegmentation of the Si II image (Lin et al. 2005). These numerically determined supergranular boundaries can be readily compared to the intensity pattern observed (Fig. 2*a*), as well as the heuristic boundaries that have previously been published for the 1996 September 22 SUMER observations (see Hassler et al. 1999, Fig. 3).

In the large majority of the analysis to follow, we will need to artificially thicken the computed watershed boundaries in order to produce distributions of quantities belonging to the supergranular cell boundaries and interiors. The thickening is simply achieved by allowing the boundary mask (Fig. 2*b*, *white contours*) to expand by 1 pixel on either side. This effectively forces the boundary thickness to be 3 pixels (9″), which appears to be consistent with those observed. An analysis of the derived supergranular network boundaries and their expansion above the photosphere is provided by Aiouaz & Rast (2006).

3. DATA ANALYSIS

In this section we use Figures 3–11 to investigate the multithermal structure of the solar transition region, its relation to the supergranular network structure and magnetic environment threading the plasma using a single set of high-quality SUMER observations. To clarify the details of the analysis, we break this section of the paper into three parts, as follows: the first discusses the comparison of the spectroscopic data [Si II, C IV, and Ne VIII] from the 1996 September 22 quiet-Sun and 1999 November 6 coronal hole rasters; the second places the spectroscopic data in context with the photospheric magnetic field and simple diagnostics derived from it, while the third combines and compares the key factors of the analysis of the spectroscopic and magnetic diagnostics in the two plasma regimes.

3.1. *Spectroscopic Data: Quiet Sun versus Coronal Hole*

Figures 3 and 4 show the Si II, C IV, and Ne VIII intensity and Doppler velocity rasters of the quiet Sun and coronal hole rasters of 1996 September 22 and 1999 November 6, respectively. The panels of each figure show the watershed boundaries computed from the Si II intensity. Comparing Figures 3*b* and 4*b*, we see that the Si II Doppler velocities on the boundaries are predominantly redshifted by about 2 km s^{-1}, while the -1 km s^{-1} blueshifts in the interiors may represent convective "overturn" flow, although this measurement is comparable to the ± 1 km s^{-1} uncertainty in the Doppler velocity measurements (Davey et al. 2006).

The C IV emission in Figures 3*c* and 4*c* forms an apparently high-intensity contrast proxy for the chromospheric network (also noted by Aiouaz et al. 2005), while, for Fig. 4*c*, the emission inside the coronal hole appears weaker and the cell interiors are better defined (apparently darker, even in the logarithmic scale of the image). From Figure 3*d* we see that there are very few locations in the field of view where the C IV emission is blueshifted (4% of the total number of pixels in the image have blue shifts greater than 3 km s^{-1}), and these locations appear to surround the bright network vertices. However, in the coronal hole C IV Doppler velocity image (Fig. 4*d*) there is an apparently larger amount of blueshifted C IV plasma inside the coronal hole boundary (21% of the number of image pixels inside the coronal hole boundary contour), but the locations appear to show no significant correlation with the network, except that very few exist

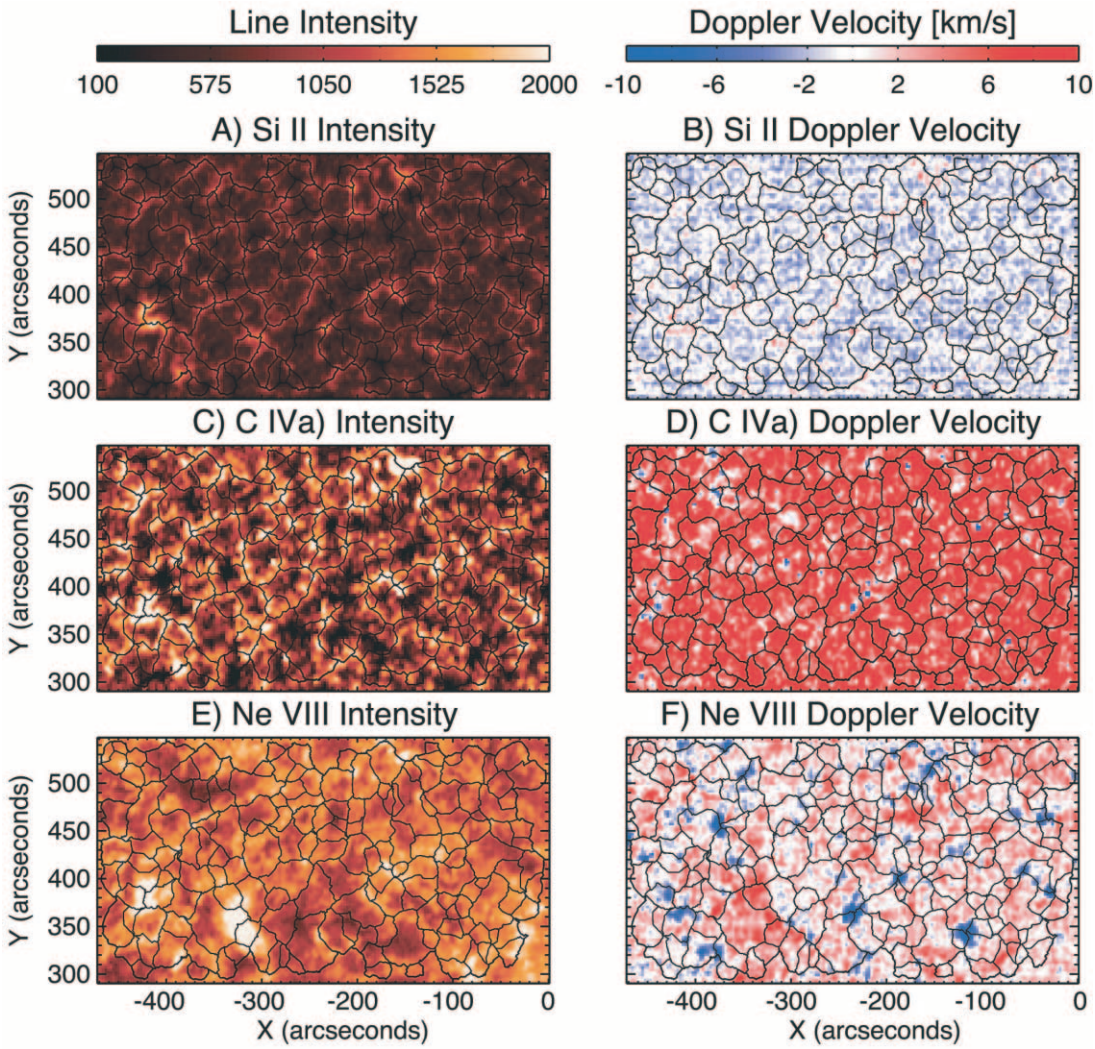

FIG. 3.—SUMER raster images of the quiet-Sun region observed on 1996 September 22 (intensity images on the left with the corresponding line Doppler shift on the right). In each of the panels we show the inferred supergranular cell boundaries that are determined from the Si II intensity image as thin black lines.

on the derived supergranular boundaries. This is remarkably close to previous measurements from sounding rocket flights by Dere et al. (1989), who demonstrated that 26% of the observed coronal hole showed C IV blueshifts, while only 7% of the quiet-Sun region did. In fact, using the distribution of C IV-boundary distances shown in Figure 5, we can show that the large C IV blueshift regions have a mean distance of 6.7 Mm from the supergranular boundary, and only 8% lie within 2 Mm of the boundary.

The Ne VIII intensity in Fig. 3*e* is almost uniformly bright and appears to have lost the strongly contrasting emission from the chromospheric network. Figure 4*e* shows a marked decrease of the Ne VIII intensity in the coronal hole. Clearly the most dramatic change in the spectroscopic data between the quiet Sun and coronal hole lies in the amount and locations of the blueshifted Ne VIII plasma (compare Figs. 3*f* and 4*f*). While the quiet Sun shows blueshifted regions that overlie bright supergranular vertices (at the junctions of three or more supergranules that radiate strongly in Si II; e.g., Hassler et al. 1999; Xia et al. 2004; Tu et al. 2005b), there is a large portion of the coronal hole plasma that is blueshifted. The coronal hole Ne VIII blueshifts are not solely located at the bright supergranular vertices, and there appears to be little or no clearly visible tie to the supergranular network pattern (contrary to the result of Hassler et al. [1999], but consistent with the recent analysis by Aiouaz et al. [2005] of the same SUMER raster data). It is the profound and apparently (physically) coupled differences between the emission and Doppler patterning of the quiet Sun and coronal hole in the 100,000 K (C IV) and 600,000 K (Ne VIII) transition region plasma that have provoked this investigation.

Figure 6 shows the distributions of the C IV spectroscopic diagnostics in each plasma regime. Figures 6*a* and 6*b* show the intensity and Doppler velocity distributions in the quiet Sun (*red histogram*) and coronal hole (*blue histogram*) data. Figures 6*c* and 6*d* show how these distributions break down into their supergranular network and supergranular interior components based on the watershed segmentation masks (see figure legend for histogram labeling). From Figures 6*a* and 6*b*, we see that the C IV emission inside the coronal hole is reduced by almost 30% (*blue histogram*) compared to that of the quiet Sun (*red histogram*), while the corresponding Doppler velocities change from $\sim$4 to $\sim$7 km s^{-1}. The C IV emission contrast is most obvious in the cell interiors of the coronal hole (Fig. 6*c*), where the emitted intensity drops by a further 20% from the supergranular boundary value. The contrast change between quiet-Sun supergranular boundaries is not as profound (on the logarithmic scale used) but is very apparent in Figures 3 and 4. Further, we see that

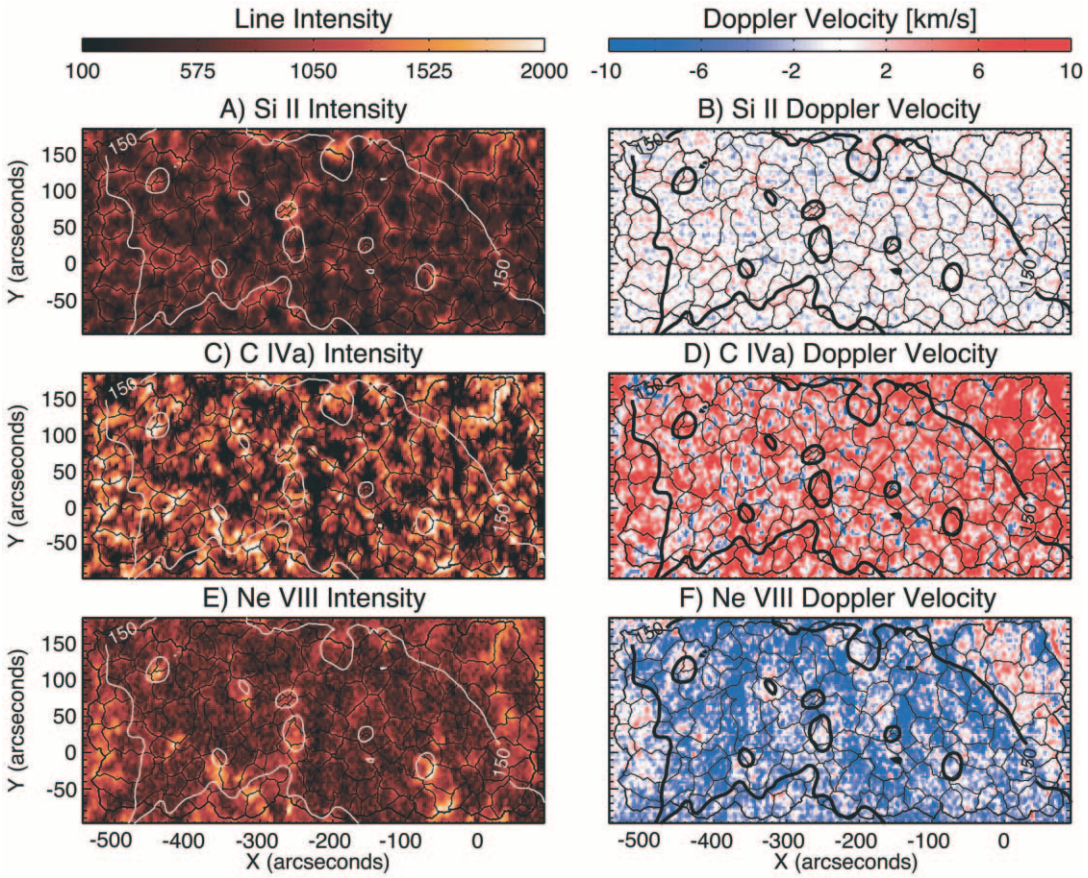

FIG. 4.—SUMER raster images of the equatorial coronal hole region observed on 1999 November 6 (intensity images on the left with the corresponding line Doppler shift on the right). In each of the panels, we show the EIT coronal hole boundary and the inferred supergranular cell boundaries determined from the Si II intensity image as thin black lines. On each panel, we show the coronal hole boundary as inferred from the EIT Fe XII emission (at a level of 150 DN) from the EIT Fe XII 195 Å image taken closest to the start of the SUMER raster scan.

the C IV Doppler shifts on the supergranular boundaries are typically stronger (by $\sim$1 km s^{-1}) than those in the supergranular interiors in both cases. These points are consistent with previous comparisons (Gebbie et al. 1981; Dere et al. 1989; Warren et al. 1997; Wilhelm et al. 2002). We note that the presence of the large pervasive redshifts on the supergranular boundaries (of the quiet Sun and coronal hole regions alike) is indicative of subspatial resolution magnetic fields advected there by the convective flow field (Berger & Title 2001), granular flow–driven reconnection (Hansteen et al. 1996), or downward propagating acoustic waves (Hansteen 1993).

Figure 7 shows a set of scatter diagrams relating the C IV Doppler velocities with their Ne VIII counterparts (*top row*) and the C IV intensities (*bottom row*) in the supergranular cell interiors of the coronal hole interior, exterior and quiet Sun.[2] From Figure 7*a* we see a strong correspondence between the coronal hole C IV and Ne VIII blueshift locations. Close inspection of the panel (and the spectroscopic images) shows that a very large fraction (92%) of the large C IV coronal hole blueshift locations underlie Ne VIII blueshifts of the same or higher magnitude. This, we feel, indicates a direct physical connection between the two. Conversely, in the quiet Sun, we see that very few of the pixels with C IV blueshifts underlie Ne VIII blueshifts; as we have stated above the large quiet-Sun C IV blueshifts neighbor the large supergranular vertex Ne VIII blueshifts instead, a point that we substantiate in the following subsection. In the coronal hole exterior (Fig. 7*b*) and quiet Sun (Fig. 7*c*), we see that the mean C IV supergranular cell interior Doppler shift has indeed increased by about 3 km s^{-1} (consistent with Gebbie et al. 1981; Dere et al. 1989; Wilhelm et al. 2002, and Fig. 6), with corresponding mean Ne VIII velocities in the coronal hole exterior of $\sim$0 km s^{-1} and quiet Sun of $\sim$1 km s^{-1}, respectively. Note that there are very few blueshifted pixels in either of the latter regions. From Figure 7*d* we see that the strongest blueshifted C IV pixels occur in the darkest portions of the coronal hole—noting again that the mean coronal hole supergranular interior C IV intensities are reduced by about 40% compared to their counterparts in Figures 7*e* and 7*f* (see Fig. 6). Dere et al. (1989) noted no distinct correlation of the C IV blueshifts with bright intensity features. Since we see that the C IV blueshifts in the coronal hole exist predominantly in the (dark) supergranular interiors, we can only speculate that a lack of spatial correspondence to anything bright made them appear to be insignificant.

3.2. *Spectroscopic Relationship to the Magnetic Topology*

Clearly, the relationship between the Doppler shift and intensity patterning of C IV and Ne VIII in both regions is complex, but their behavior appears to be strongly coupled. We now investigate how the magnetic field observed in each region can add further evidence to help us explore the magnetic connection between the

[2] We make a distinction here with coronal hole exterior and interior of the 1999 November 6 data to demonstrate that (statistically at least) the coronal hole exterior (the region outside of the *SOHO* EIT 150 DN contour) behaves identically to the quiet Sun data of 1996 September 22, as we would expect.

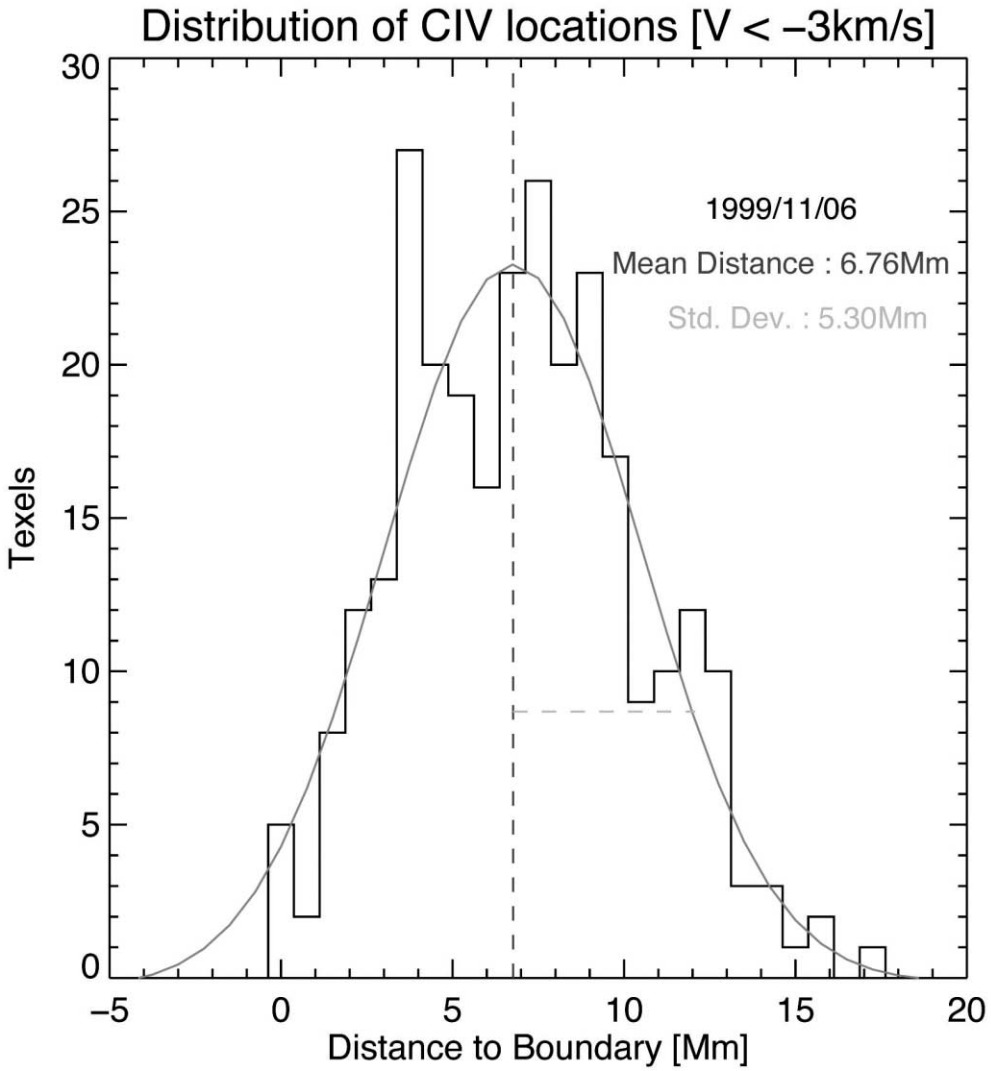

FIG. 5.— Distance distribution of the larger C IV blue Doppler shifts (< -3 km s^{-1}) compared to the watershed segmentation supergranular boundary for the equatorial coronal hole raster of 1999 November 6. Using a method that has previously been employed to identify and locate extreme ultraviolet "bright points" in EIT images (McIntosh & Gurman 2005), we locate regions of large blueshift and measure their distance from the inferred supergranular boundary. We see that only 8% of the strong C IV blueshifts lie within 2 Mm of the boundary. They have a mean distance of 6.76 Mm. [*See the electronic edition of the Journal for a color version of this figure.*]

cool (Si II) and hot (Ne VIII) plasmas. This allows us to compare our results with previous investigations of the magnetic environments in coronal holes and the quiet Sun (Hassler et al. 1999; Dammasch et al. 1999; Xia et al. 2003; Tu et al. 2005a; Aiouaz et al. 2005).

Figures 8 and 9 show the comparison of two different models of the magnetic environment with the Doppler velocity maps of C IV and Ne VIII in the quiet Sun and coronal hole, respectively. Figures 8*a* and 8*b* and 9*a* and 9*b* show two representations of the underlying photospheric magnetic field at the start of the SUMER raster observation: (A) the raw MDI magnetogram and (B) the same magnetogram smoothed by a circular filter of radius of 20 Mm ($\langle B_{||} \rangle_{r=20}$; McIntosh et al. 2006). The latter shows the presence of net magnetic field polarities at a spatial scale commensurate with a supergranule. The fine black line in Figures 8*b* and 9*b* shows the magnetic neutral line where positive and negative polarities cancel. Directly comparing Figures 8*b* and 9*b*, we see that the coronal hole has considerably more positive magnetic flux than the mixed polarity (zero mean field) quiet Sun.

In Figures 8*c* and 9*c* we show the angle to the vertical of the extrapolated linear force-free field (Alissandrakis 1981; Gary 1989) at 2 Mm in the atmosphere, just above the probable formation height of the Ne VIII emission (Tu et al. 2005a, 2005b). By isolating angles greater than 35° in this region, we attempt to show the locations of "coronal funnels" invoked largely to explain the patterning of the Ne VIII blueshifts in SUMER rasters (Xia et al. 2003, 2004; Tu et al. 2005a, 2005b). We see that the funnels, more often than not, coalign with the bright Si II emission at bright supergranular vertices (see, e.g., Figs. 2 and 3) and overlie magnetic flux regions of the same polarity as the dominant magnetic polarity of the supergranule. Comparing the funnel locations with the C IV blue shift locations (Figs. 8*e* and 9*e*), we see little correspondence at all; the C IV blueshift regions lie immediately outside the funnels. Using the data in Fig. 8*g*, we see that, in the quiet Sun, the funnels outline more than 65% (±5% for estimated errors in coalignment with MDI) of the blueshifted material in Ne VIII (Fig. 10). However, in the coronal hole (Fig. 9*g*) the correspondence between funnels and blueshifted Ne VIII plasma drops dramatically to 35% (±5%; Fig. 11).

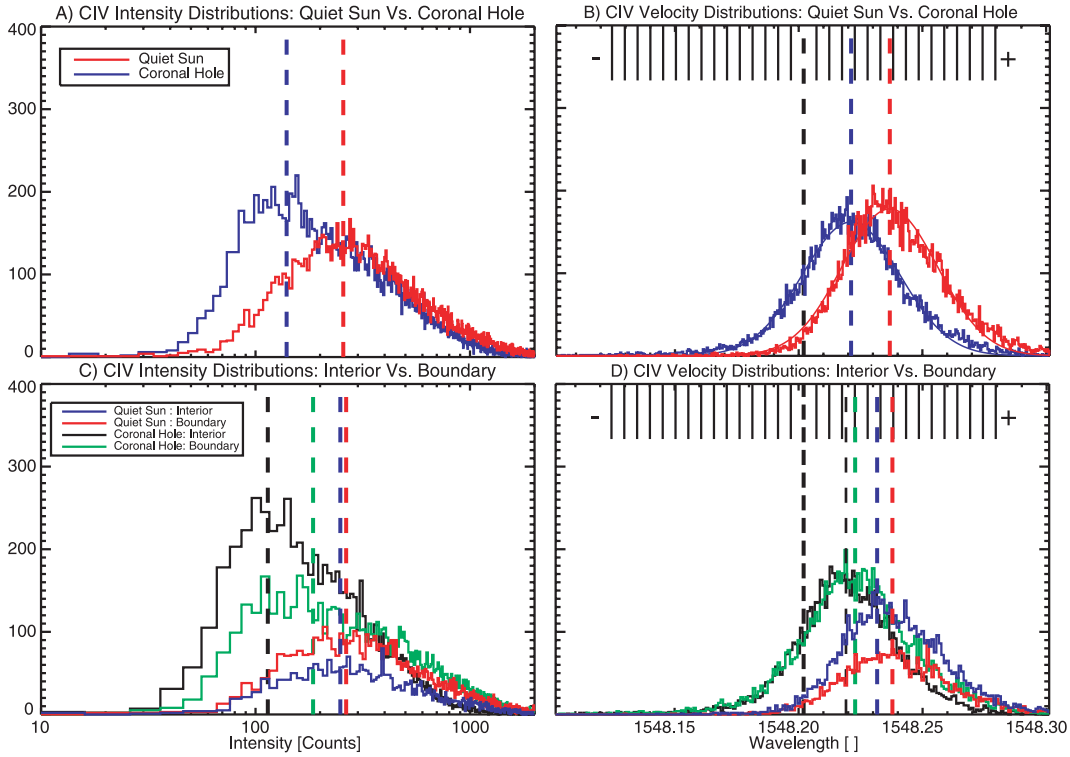

FIG. 6.— Distributions of the C IV intensities (*left column*) and Doppler velocities (*right column*) for the data presented in Figs. 3 and 4. While the top row of pixels shows the distributions partitioned for the entire coronal hole and quiet-Sun regions, the bottom row shows the breakdown of these into the supergranular cell boundary and interior components. In each panel, the vertical dashed lines mark the position of the distribution mean of the same color and thickness. In (*b*) and (*d*) the thick black dashed line indicates the rest wavelength of the emission line, and the vertical ticks mark off 1 km s^{-1} increments in the Doppler velocity of the line. Compare with Fig. 11 of Davey et al. (2006).

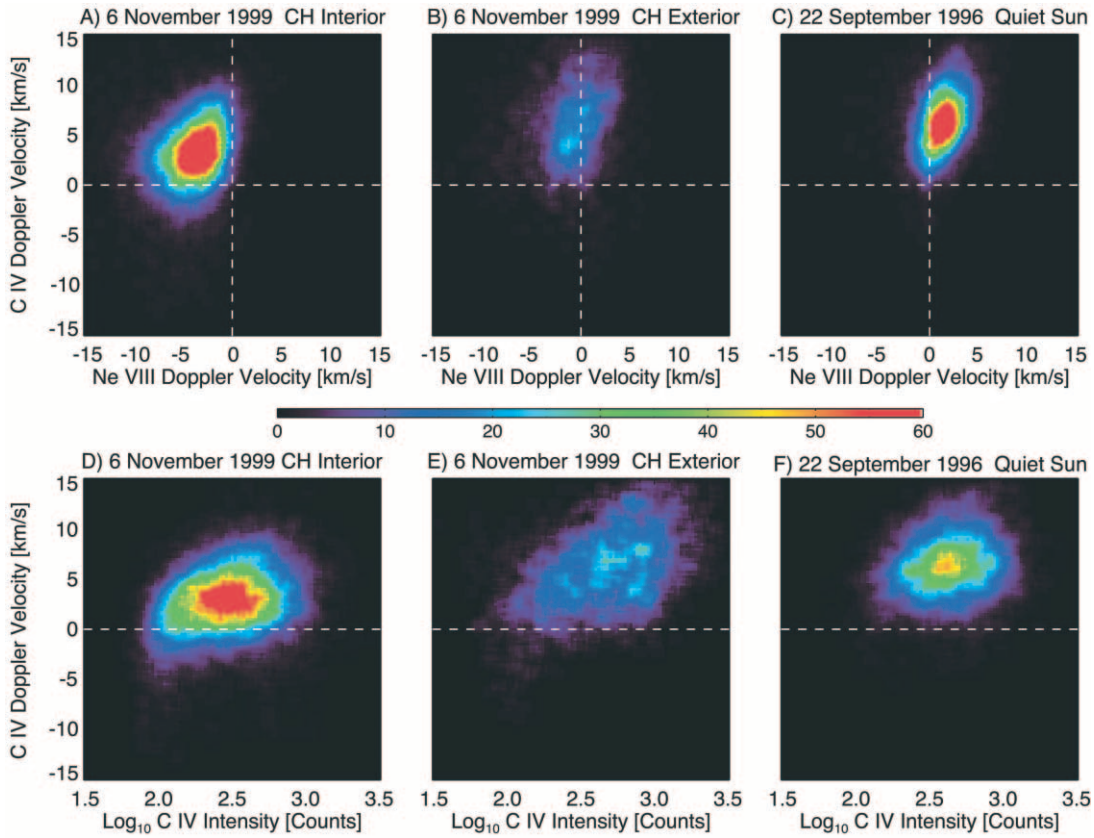

FIG. 7.— Scatter diagrams to quantify the correspondence of C IV Doppler velocities with those of Ne VIII (*top row*) and the logarithm of C IV intensity (*bottom row*) for supergranular interiors. From left to right the columns correspond to quantities that are in the computed supergranular network cell interiors inside the 1999 November 6 coronal hole (*left*), outside the coronal hole (*center*), and for the 1996 September 22 quiet-Sun raster (*right*). The last two columns should behave identically.

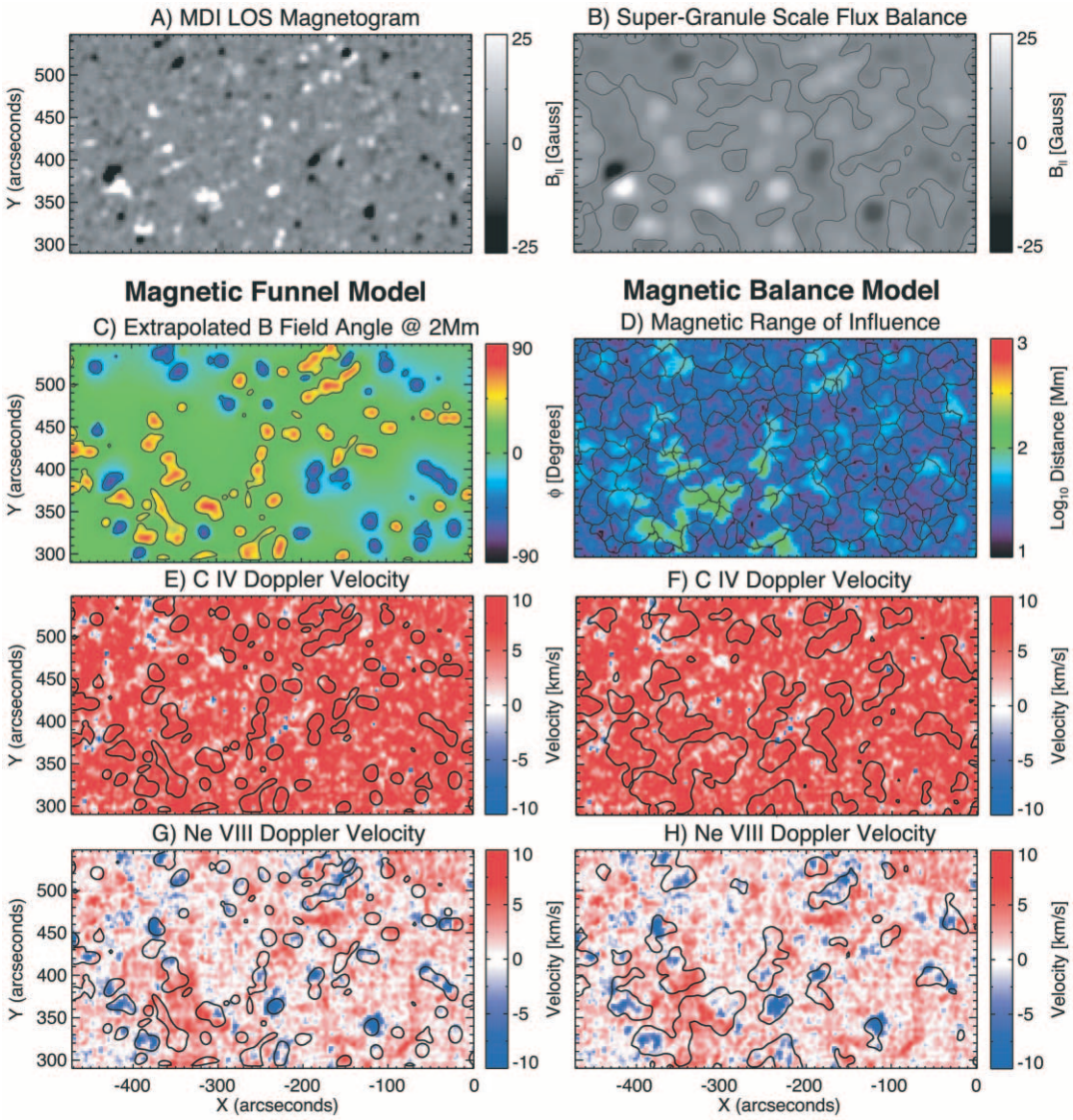

FIG. 8.—Comparison of two simple magnetic models and their correlation to the C IV and Ne VIII Doppler velocity maps from the quiet-Sun SUMER raster of 1996 September 22. We show the MDI line-of-sight magnetogram (*a*) and the 20 Mm smoothed MDI line-of-sight magnetogram ($\langle B_{||} \rangle_{r=20}$; McIntosh et al. 2006). In (*c*) we show the extrapolated magnetic field angle (to the vertical) at a height of 2 Mm. We identify regions where the absolute value of the field angle is greater than or equal to 35° as belonging to a magnetic funnel with sold black contours. These same regions are then compared to the C IV and Ne VIII Doppler velocity maps ([*e*] and [*g*]). In (*d*) we show the MRoI (McIntosh et al. 2006) map derived from the magnetogram in (*a*) along with the watershed boundaries to demonstrate the net magnetic flux on any particular cell. We isolate regions where the MRoI is greater than 50 Mm with solid black contours in (*f*) and (*h*).

Figures 8*d* and 9*d* show a simple diagnostic of the degree of magnetic imbalance present, the magnetic range of influence (MRoI; McIntosh et al. 2006). The MRoI is an estimate of the radial distance needed from a particular magnetic flux concentration to meet enough flux of the opposite polarity to balance and is computed from the full disk (full spatial resolution) MDI magnetogram. The MRoI can be thought of as a crude measure of how open (large MRoI) or closed (small MRoI) the region is. In the quiet Sun, the MRoI map shows few locations greater than 100 Mm; these, however, coalign well with the vertex or coronal funnel locations and thus the regions of strong Ne VIII blueshift. Conversely, in the coronal hole, we see that there are few locations where the MRoI map drops below 100 Mm, and the regions of large MRoI appear to correspond with the global structure of the Ne VIII blueshift pattern (McIntosh et al. 2006, Fig. 3). Similarly, the vast majority of C IV blueshifts occur in regions where the MRoI is greater than 100 Mm and there is net imbalance in the magnetic field. We speculate that the existence of large-scale regions of unbalanced magnetic fields in the coronal hole, and the energy that they contain, is important in setting the amount of energy released and hence the magnitude of the blue shifts observed.

3.3. *Key Points in the Analysis*

Before proceeding we would like to summarize the key points of the analysis presented so far:

1. In the coronal hole the C IV and Ne VIII supergranular interior emission and boundary emission drop by ~40% compared to their values in the quiet Sun. Further, there is a strong correlation between blueshifts in C IV and Ne VIII, and regions of lowest emission. Both are well-observed correlations (e.g., Dere et al. 1989; Wilhelm et al. 2002; Aiouaz et al. 2005).
2. In the quiet Sun 65% of the Ne VIII blueshifted plasma lies in regions of unbalanced magnetic flux at bright supergranular vertices, so-called coronal funnels (e.g., Xia et al. 2003, 2004; Tu et al. 2005a, 2005b).

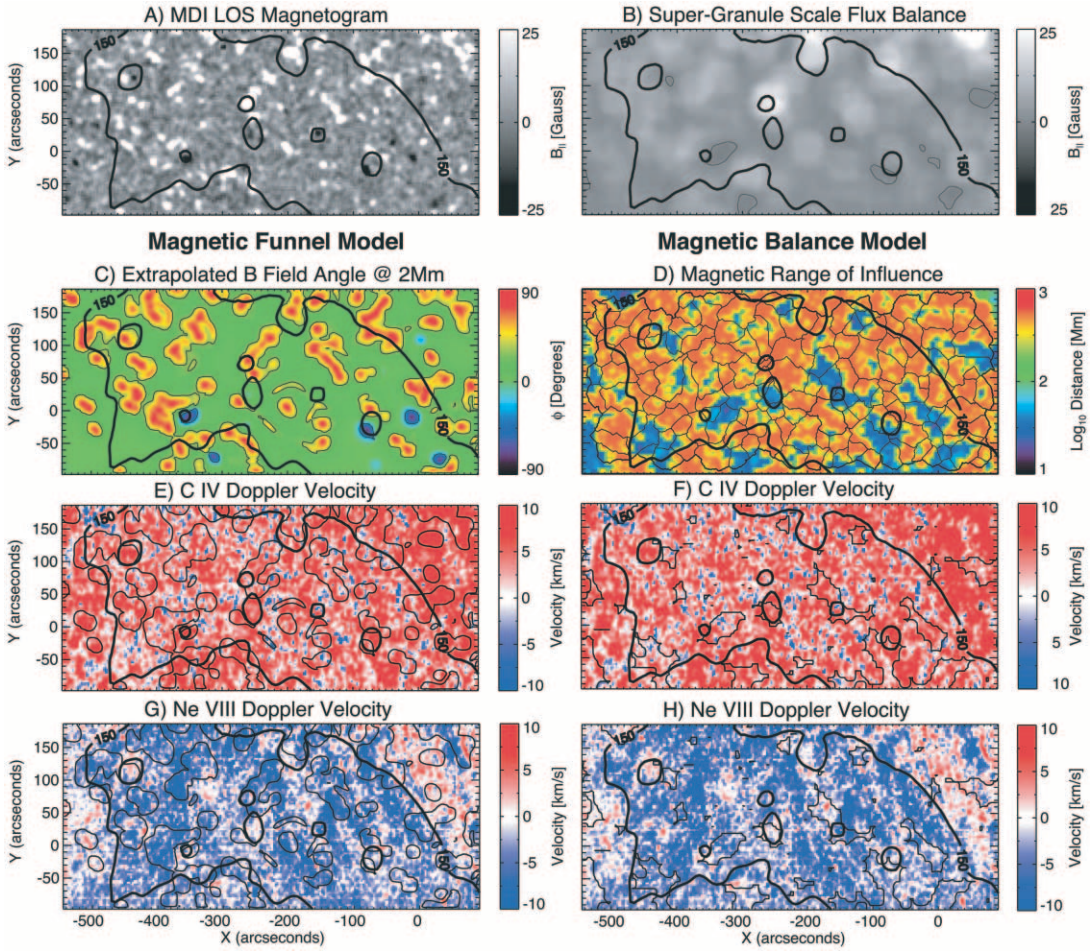

FIG. 9.— Same as Fig. 8, except that we now compare the simple magnetic models with the C IV and Ne VIII Doppler velocity maps from the SUMER equatorial coronal hole raster of 1999 November 6. Again, we illustrate the coronal hole boundary by drawing the 150 DN contour in the EIT Fe XII 195 Å emission.

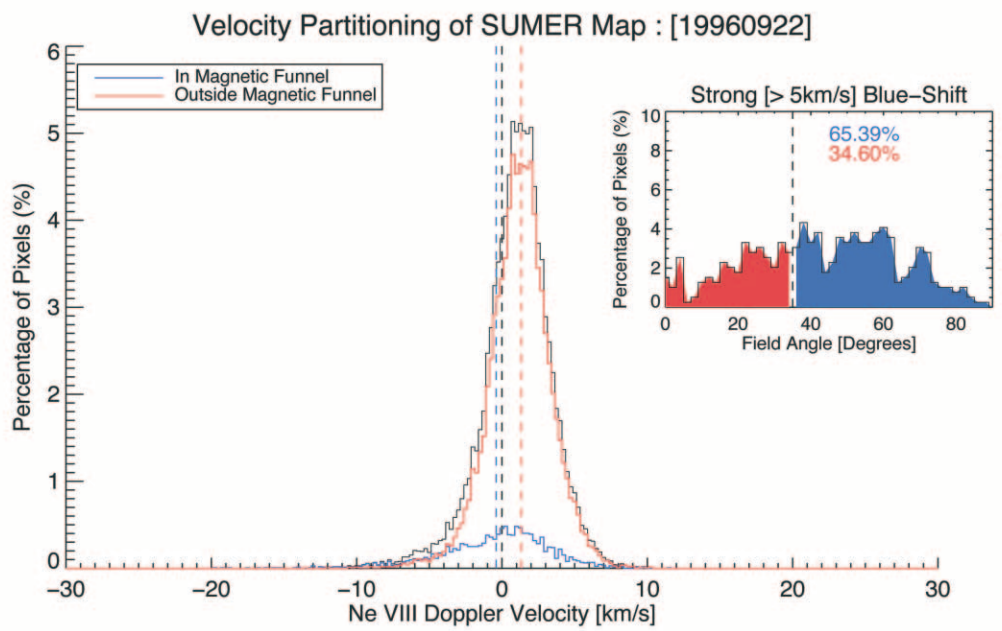

FIG. 10.— Velocity partitioning plot for the quiet-Sun SUMER raster of 1996 September 22. In the main body of the figure, we show the distribution of the pixels in the Ne VIII Doppler shift map along with those which are inside magnetic funnels (*blue*) and those that are outside (*red*). The inset plot shows the distribution of large (<-5 km s^{-1}) Ne VIII blueshifts by field angle. We see that ~65% of the pixels with large blueshifts occur in funnels and, as such, back up the model of (Xia et al. 2003; Tu et al. 2005b) in the quiet Sun.

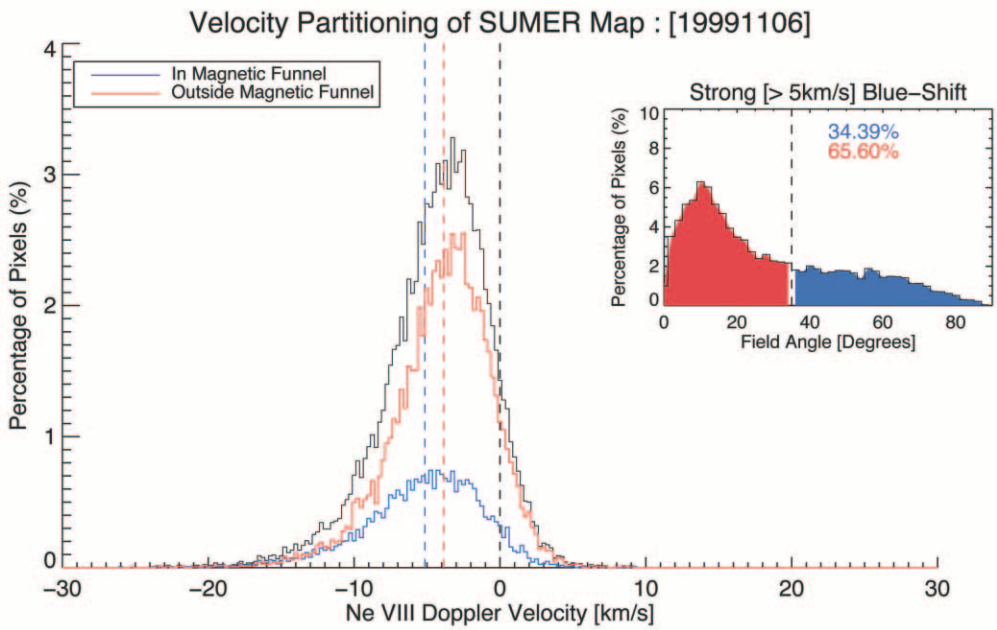

FIG. 11.— Same as Fig. 10, but now we perform the same test for the equatorial coronal hole region of 1999 November 6 and can see that by far the largest portion (65%) of strong Ne VIII blueshifts do not occur magnetic funnels.

3. In the coronal hole only 35% of the Ne VIII blueshifted plasma lies at bright supergranular vertices. The remaining 65% of the Ne VIII blueshifted plasma lies in regions of unbalanced magnetic flux away from bright network vertices. Further, we agree with the analysis of Aiouaz et al. (2005) that the additional Ne VIII blueshift regions are not directly correlated with the observed network structure, contrary to the earlier analysis of Hassler et al. (1999).

4. There is a larger fraction of C IV blueshifting pixels (21%) in the coronal hole compared to the quiet Sun (4%). The vast majority of C IV blueshifts (in both cases) occurs in regions of unbalanced magnetic flux. This dramatic change in the fractional coverage of C IV blueshifts matches a suite of sounding rocket C IV observations (e.g., Dere et al. 1989).

5. There are very few locations of C IV blueshift on supergranular boundaries. By far the higher percentage (96%) is located to the interior side of supergranular boundaries; less than 10% of the C IV blueshifts is within 2 Mm of the boundary. In the quiet Sun the C IV blueshifts neighbor bright supergranular vertices.

6. Some 92% of coronal hole C IV blueshifts underlie Ne VIII blueshifts of comparable or larger amplitude. This is compared to only 5% outside in the quiet Sun. This implies a physical (magnetic) connection between the blueshifted 100,000 and 600,000 K plasmas in the transition region. These connected blueshift regions almost uniquely occur in regions of significant magnetic unbalance.

4. DISCUSSION

We have used SUMER raster observations of an equatorial coronal hole and a quiet-Sun region to investigate the relationships between the multithermal emitted spectral line intensities and Doppler velocities, the supergranular patterning of the chromospheric network, and the magnetic environment of the plasma. The pictorial and statistical relationships developed for the transition region emission lines of Si II, C IV, and Ne VIII suggest that the key to understanding the physical mechanism responsible for coronal heating, as well as the acceleration of the solar wind, rests on the correct physical interpretation of the Doppler velocity patterning present in the C IV and, in particular, the relationship of the strong C IV blueshift regions with the supergranular boundaries and magnetic polarity balance on supergranular spatial scales. While most of the previous analyses (e.g., Wilhelm et al. 2002; Xia et al. 2003, 2004; Tu et al. 2005b), have presented the emission and Doppler velocities of C IV pictorially, few have compared the C IV Doppler velocity patterning with that observed in Ne VIII. The present analysis complements the past results, but provides a new, self-consistent interpretation of the observations.

Figure 12 introduces three simple cartoons in an effort to explain the connection between the magnetic carpet and the multithermal spectroscopic patterning observed by SUMER in the quiet Sun and in coronal holes. These cartoons are derived from an already published, idealized model of a supergranular cells (Wang 1998) and cross sections (Priest et al. 2002) of the cell that are representative of the global magnetic environment in a coronal hole (Fig. 12*a*) and the quiet Sun (Fig. 12*b*).

The top cartoon (*a*) illustrates the likely situation in a coronal hole. The small (spatial) scale flux elements anchored in the supergranular boundary (*shown in red*) are effectively open to interplanetary space because they have the same magnetic polarity as the bulk of the coronal hole. As the small, recently emerged magnetic dipole (*blue*) is advected to the boundary, the leading polarity of the flux begins to reconnect with the anchored element, creating a new magnetic topology in the supergranular interior (*green*). A portion of the energy released by the reconnection quickly begins to evaporate cool chromospheric material into the topology (see, e.g., Yokoyama & Shibata 1998; Czaykowska et al. 1999), where the bulk of the remaining energy is released in the form of kinetic energy. The established flow results in the observed correlation of blueshift in C IV and Ne VIII given above and to the supergranular interior side of the topological X-point. The blue dashed lines in the cartoons demonstrate the places in

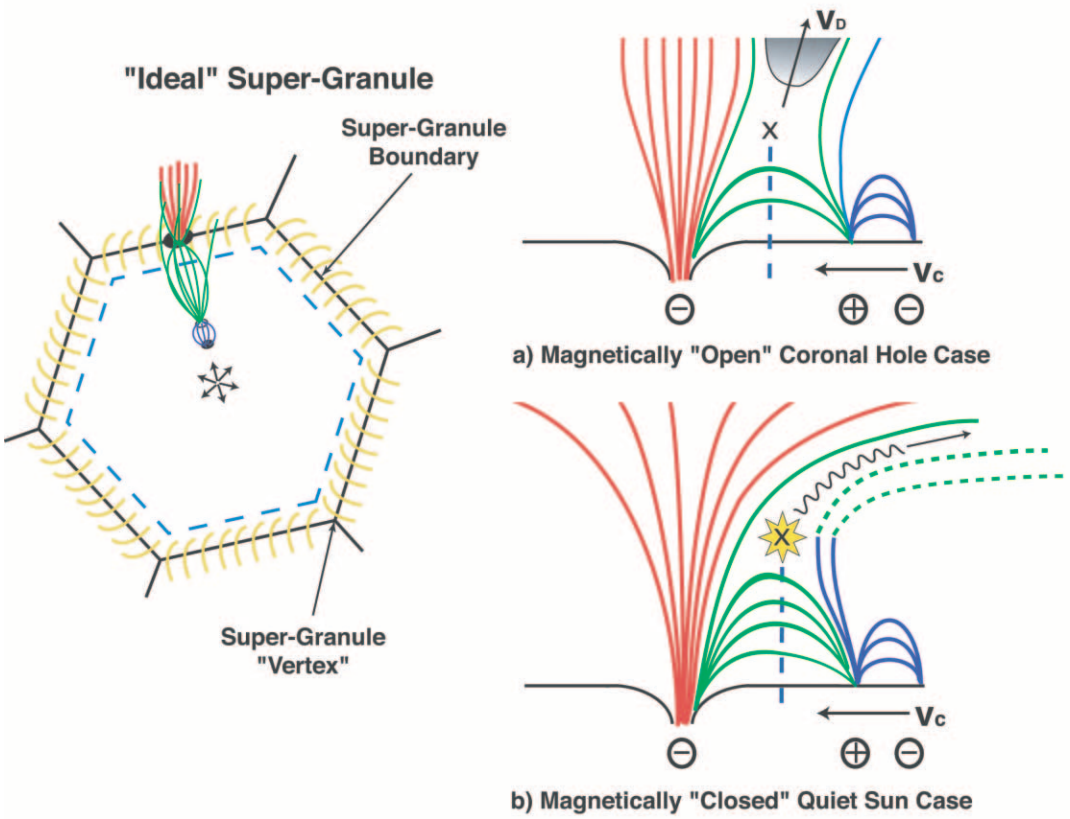

FIG. 12.—Cartoon of a supergranular cell and the action of the magnetoconvection driven magnetic carpet in the magnetically "open" network (coronal hole) case (*a*) and the magnetically "closed" network (quiet sun) case (*b*). In each case the network boundary flux is shown in red, while the emerging magnetic dipole is in blue. The green lines of force are those resulting from the reconnection of the emerging advected dipole and the network boundary flux. The "X" marks the reconnection X-point where the bulk of the stored energy in the field is released. In case (*a*) with no overlying closed magnetic field, the magnetically released material can "escape" to become a tributary to the solar wind while, in case (*b*), with overlying closed quiet Sun the magnetic field releases the bulk of its energy thermally into the loop structure. The blue dashed line indicates the potential locus of C IV blueshift. These cartoons are adapted from those published by Wang (1998) and Priest et al. (2002).

this ideal model where the C IV blueshift regions might occur and qualitatively agrees with the determination from the actual data. The newly created flux topology in the coronal hole supergranular interior will then tend to expand to the cell interior, where the net atmospheric pressure is lower, consistent with the predictions of Schrijver & Title (2003). We predict that the actual location, lifetime, and strength of the blueshift in the coronal hole will depend on the magnitude of the dipole being advected, its size relative to the field on the boundary and the net imbalance of the field in the cell. This cannot be tested with the observations at hand, but we note that the qualitative dependence of the Ne VIII Doppler pattern and the MRoI map add weight to this interpretation.

In the quiet Sun (Fig. 12*b*), we assume that the supergranular boundary–anchored magnetic flux (*red*) closes with an opposite polarity piece of magnetic flux on a nearby supergranule (Fig. 3), such that there is very little probability that any arcade created in the supergranular interior can open into interplanetary space (McIntosh et al. 2006). The convection-driven reconnection of the emerging magnetic dipole creates a new magnetic topology (*green*) in the supergranular interior that is bound below the preexisting intercell magnetic loop arcade. We anticipate that, as the dipole is advected to the boundary and the reconnection progresses, the bulk of the released energy must result in the evaporative mass-loading of the created arcade and thermal heating of the plasma contained in it, since little of it can be rapidly converted into plasma outflow. In this case, we would expect to see very few C IV blueshifts. We presume that the reconnection sites may only be visible in locations near bright supergranular vertices, i.e., where the magnetic field is locally dominated by one polarity (bright network vertices) and so is effectively radial (or open) (e.g., Lites 2001). The thermal heating and apparent invisibility of the reconnection X point in the newly created arcade can qualitatively explain the observed increase in emission and resulting increase in contrast of the supergranular boundaries visible in the quiet Sun.

We can probabilistically explain the dearth of C IV blueshift regions in the quiet Sun compared to the coronal hole. In the coronal hole, there is net imbalance in the magnetic field and the probability of dipole annihilation increases with the degree of magnetic imbalance. As such, the dipole can be annihilated anywhere in the coronal hole cell, but it has a significantly higher probability of destruction closer to the boundary (where the net magnetic flux is larger). In the quiet Sun, where the supergranular cell has a near-zero mean field, the probability of immediately annihilating the advecting dipole is almost negligible; hence the dipoles will live much longer and will probably have to migrate significantly closer to the supergranular boundaries (or vertices) before they meet enough imbalance in the magnetic field to be destroyed. Further, we believe that the relentless magnetoconvection-driven reconnection could explain the prevalent transition region redshift (e.g., Warren et al. 1997). We suspect that the same process of radiative cooling of down-flowing material (Müller et al. 2005), observed as "coronal rain" (e.g., Foukal 1976, 1977;

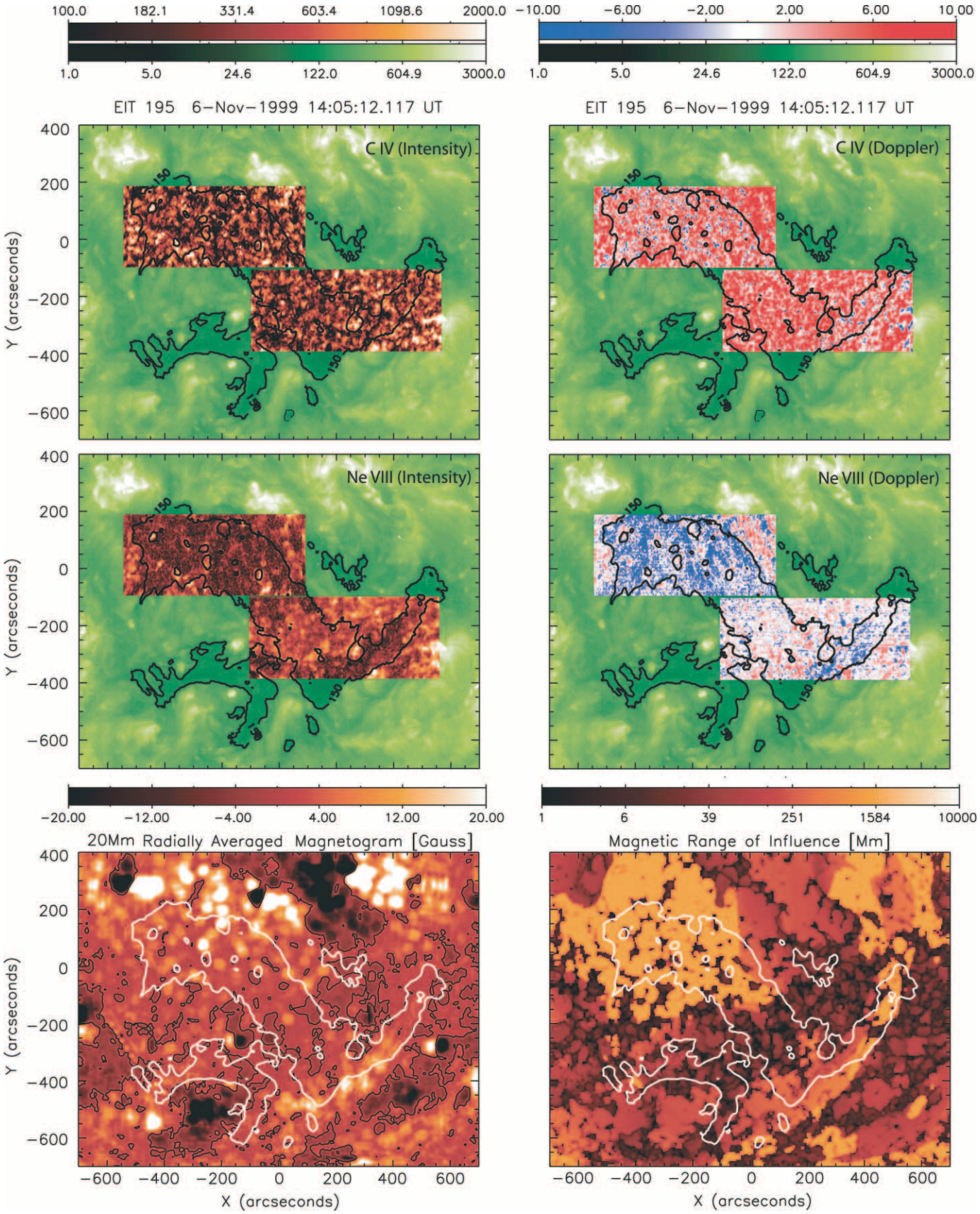

FIG. 13.—Adaptation of Fig. 3 of McIntosh et al. (2006). The top two rows show the SUMER C IV 1548 Å and Ne VIII 770 Å integrated line intensities (units: counts) and Doppler-velocities (km s^{-1}), respectively. The bottom row shows the supergranular radially averaged magnetic field strength ($\langle B_{||} \rangle_{r=20}$; gauss) and the MRoI (megameters). On each of the panels in the figure, we show the EIT 195 Å 150 DN contour to outline the coronal hole region. In addition, in the bottom left panel, we show the thin black contour that designated the magnetic "neutral line," where $\langle B_{||} \rangle_{r=20} = 0$ G.

Ionson 1978; Bruner & Lites 1979; Athay et al. 1980) in the vicinity of sunspots over the limb is largely responsible for the differences in the coronal hole and quiet-Sun C IV redshifts (Figs. 3, 4, and 13). Consider the fact that, in the quiet Sun, it appears that much less of the material ejected into the magnetic topology in the upper atmosphere can "escape," and therefore, under the influence of gravity, it will fall, creating a "coronal drizzle" in the supergranular cell. This effect will be less prevalent in the magnetically open coronal hole *if* the ejecta form the basis of the solar wind and do not return. We also should note that it is entirely possible that acoustic waves are also present in the downflowing material and contribute to the net redshift observed (Hansteen 1993). While we cannot tell using the present observations, recent research has demonstrated the connection of transient, propagating low-frequency (<5 mHz) magnetoacoustic waves in spicules (De Pontieu et al. 2004) and around supergranular cell boundaries (Jefferies et al. 2006) may form a ready source of these waves.

While we have largely chosen to neglect the discussion of Ne VIII blueshifts at bright supergranular vertices, they form an important component of the complete physical description of the observations that we present. The occurrence of coronal magnetic funnels is clearly demonstrated, having impact primarily on the quiet Sun (e.g., Fig. 8). The very close proximity of the C IV blueshift regions in the quiet Sun to the magnetic funnels suggests that the mechanism invoked to supply mass and energy to the funnel (e.g., Xia et al. 2003) is correct and akin to the magnetic carpet–driven "magnetic exchange reconnection" model of Wang (1998), which is thought to load and accelerate mass in a "polar plume." If we can assume that the Ne VIII blueshifts observed at bright supergranular vertices are near cousins of polar plumes, the additional magnetic flux concentrations on and around the supergranular boundaries in the coronal hole are of significantly smaller spatial scale ($\sim$1000 times smaller at a fraction of an arcsecond in radius; Berger & Title 2001), and as such one million times smaller in area—a spatial distribution of microplumes (μ-plumes). Although it is clearly beyond the scope of this article, we draw the reader's attention to the spatial distribution of the spectroscopic characteristics of these ejecta and similarities with other solar phenomena closely tied to supergranular structure: "spicules" (e.g., Secchi 1877; Roberts 1945; Beckers 1968; Sterling 2000; De Pontieu et al. 2004), bright and dark Hα "mottles" (e.g., Athay & Thomas 1961; Bray 1973; Bray & Loughhead 1973), "blinkers" (e.g., Harrison 1997), and "explosive events" (e.g., Innes et al. 1997; Bewsher et al. 2005). We are convinced that these phenomena are united by one underlying physical mechanism modified in spectral output by the topology of the magnetic field on the supergranular and global scales (e.g., Madjarska et al. 2006; McIntosh 2006).

5. COUPLING TO THE GLOBAL SCALE OF THE SOLAR ATMOSPHERE

In the previous sections we have focussed on small-scale ($\sim$20 Mm) energy release into the upper solar atmosphere. McIntosh et al. (2006) discussed the influence that the magnetic environment has on the Ne VIII emission and Doppler velocities. It was demonstrated that the topological nature (open or closed) and net balance of the magnetic field coupled to the emission and velocities observed for the equatorial coronal hole that was studied with SUMER from 1999 November 3–8.

From Figure 3 of McIntosh et al. (2006) we see that in the open (large MRoI; net positive field $\langle B_{||}\rangle_{r=20} \geq 5$ G) regions a strong Ne VIII blueshift was evident, which appeared to get stronger as $\langle B_{||}\rangle_{r=20}$ increased. Conversely, in places of (zero mean) closed magnetic field quiet Sun (small MRoI; net magnetic balance $\langle B_{||}\rangle_{r=20} \approx 0$ G) the blueshift pattern is replaced by one that shows a net redshift ($\sim$1 km s^{-1}), the Ne VIII blue shifts are highly localized (into "funnels"), and the emission increases visibly by a factor of 2.

Figure 13 is a simple adaptation of Figure 3 of McIntosh et al. (2006), in which we now include the global dependence of the C IV emission and Doppler velocity structures in the equatorial coronal hole (*top row*) with those of the hotter Ne VIII (*middle row*) and the two magnetic field balance diagnostics discussed above (*bottom row*). The spatial correspondence between significant Ne VIII blueshifts and regions of unbalance in the photospheric magnetic field is clear. Similarly, one can observe the increased coverage (4% increasing to 21%) of significant C IV blueshift in the same places. McIntosh et al. (2006) demonstrate that the Ne VIII Doppler velocity partitioning of the coronal hole in the central region ($x = -100'', 200''; y = -300'', -100''$; seen most clearly in the Ne VIII intensity maps) is due to the local closure of the magnetic fields (low values of MRoI and nearly balanced magnetic fields); this region is consistent with quiet-Sun energy release (enhanced Ne VIII emission, isolation of blueshifted material to bright network vertices and few C IV blueshift locations). Conversely, we also see that the open field regions determined by the magnetic diagnostics (high MRoI and unbalanced magnetic fields) point to regions that show a marked increase in the number of pixels showing significant blueshifting plasma in C IV, which, as we have shown, invariably lie below the blueshifting Ne VIII regions. We also point the reader to the spatial dependence of the C IV Doppler velocities outside the EIT 150 data number (DN) contour and in the central (Ne VIII intensity enhanced) region of the coronal hole. There is a clear increase in the magnitude of the redshift ($\sim$7 km s^{-1}) and lack of the cellular contrast (the redshift appears to fill the entire cell) that is very visible in the magnetically unbalanced portions of the coronal hole (e.g., Figs. 6 and 8).

We deduce that the global aspects of the spectroscopic signals observed (thermally) through the plasma, when compared to the magnetic flux balance, are consistent with the presence of magnetoconvection-driven reconnection as the dominant supply of energy to the plasma.

Unfortunately, the time taken to produce the two SUMER equatorial coronal hole rasters shown here ($\sim$20 hr) does not allow us to discuss the spectroscopic evolution of the transition region plasma and place it in the context of the EUV corona. This significantly limits the interpretation of the location where the EUV corona and transition region plasmas appear to be thermally partitioned, or "nested," in the central portion of the coronal hole. We know from the movie accompanying McIntosh et al. (2006) that the EUV coronal hole does not appear to evolve dramatically over the time taken to compose the rasters shown. McIntosh et al. (2006) briefly discuss the "nesting" of the coronal hole and propose that there are either two distinct coronal holes present (one to the north and one to the south with the increased emission region in the center underlying the divergent magnetic topologies of each) or that there is a very different loading and heating of the EUV plasma above the same (apparently closed) region in the transition region. While the former is the simplest explanation, we now discuss the latter.

It is possible that the magnetic environment of the EUV coronal hole is isolated from the quiet Sun and forms a perimeter isolating the region where the MRoI drops dramatically, the emission increases, and the two velocity patterns (C IV and Ne VIII) adopt their quiet-Sun form. In this case we must explain why the column depth of the plasma observed in the 195 Å EIT passband

is (almost) uniformly reduced above this region, as is the Kitt Peak Vacuum Telescope He I 10830 Å spectroheliogram equivalent width.[3] The apparent mass reduction in the region (195 Å; reduced column mass) and presence of excess nonthermal processes (10830 Å; reduction of line widths) are both consistent as coronal hole "markers" in the sense of the simple energy partitioning by the magnetic topology (open-kinetic; closed-thermal). If the closed field region is imbedded in a globally open magnetic topology, it may simply be that filling the coronal volume in that region is only possible from the quiet-Sun coronal funnels at the bright network vertices where we see Ne VIII blueshifts. From limited sources of mass, that would be difficult, and so the dispersal of mass must affect both the 195 and 10830 Å measurements in the manner observed. It was noted in McIntosh et al. (2006; and, independently, J. B. Gurman 2005, private communication) that there is a slight increase ($\sim$10 DN) in 195 Å intensity overlying this closed region, but it had very low contrast with the remainder of the coronal hole. Clearly, we are at an impasse; both of these situations are possible (as are several more), but they may only be resolved by detailed magnetic extrapolation or by watching the evolution of the coronal hole for several more rotations before and after the region was observed with SUMER. We leave this investigation for future work, but note that the global spectroscopic structure of the coronal hole did not vary over the 5 days that it was observed (Davey et al. 2006).

5.1. *Influence on the Heliosphere*

Many other markers of the coupling between the energy equation (initial energy release and distribution) and the magnetic flux balance of the solar plasma may have already been widely observed but not linked. These would appear to have an effect on the heliospheric system as a whole, but are too numerous to discuss in this paper; instead we cite a few. Systematic He I 10830 Å line asymmetries observed at the solar south pole near solar minimum (1995 October 17) have been attributed to a strong outflow ($\sim$8 km s^{-1}) of chromospheric material (Dupree et al. 1996) and occur at a time when there is a relatively strong unbalanced field at the pole. The magnetic flux that diffuses to the polar regions over the course of the solar cycle creates a long-lived "polar crown" coronal hole at solar minimum. This excessive imbalance in the polar magnetic field, we suspect, will act as a reservoir of kinetic energy for the very high speed winds observed at high heliospheric latitudes at the same phase of the solar cycle (McComas et al. 1998), while the evolving mixture of open and closed regions and the resulting energy partitioning of the plasma explain the complex heliospheric structure observed at other phases of the solar cycle (e.g., Geiss et al. 1995; McComas et al. 2000; Smith et al. 2003). One can wonder about the possible implications of this result for other observations that appear to connect coronal holes, chromospheric material and the solar wind (e.g., McIntosh & Leamon 2005; Leamon & McIntosh 2006).

The role of the global magnetic topology as a means of the controlling how the energy released into the plasma is used may have implications for the "FIP effect" (e.g., Raymond 1999; Feldman & Laming 2000; Laming 2004; Young 2005; Ko et al. 2006). The primary signature of the FIP effect is that elements with a low first ionization potential (FIP; e.g., Na, Si, Al, Ca, Fe, and Ni) are often enhanced over those with a high FIP (e.g., He, N, O, Ne, and Ar) in the slow solar wind by a factor of several, while the fast solar wind shows little or no elemental fractionation at all. We speculate that the contrast in the FIP-related enhancement of certain atomic species is tied to how and where the mass and energy are delivered to and used by the plasma. We have seen that the fast solar wind generally originates from open magnetic regions of sizable magnetic imbalance and that the energy is delivered in a mostly nonthermal (kinetic) form with mass that originates in the well-mixed chromosphere. Conversely, the slow solar wind originates in the largely closed magnetic topologies of active regions and the quiet Sun, where the latter is permeated by the small-diameter "coronal funnels" that we have discussed above. The closure of the topological features in these regions will ensure a mostly thermal energy delivery to the plasma, but will result in a complex patterning of wind properties from their spatial variability. It is possible that enhanced fractionation can take place in the plasma it is transported through the magnetic topology and eventually evaporated out of the corona and into the heliosphere in a fashion that depends on the exact magnetic topology (e.g., Schwadron & McComas 2003 and references therein). While a full investigation into the connection between the result presented in this paper and the heliospheric plasma is beyond the scope of this paper, we can see that there is significant potential.

6. CONCLUSION

Together, the *SOHO* (SUMER, EIT, and MDI) observations, statistical relationships and cartoon representations lead us to the conclusion that the observed Doppler velocity and emission patterning of the upper transition region and low solar corona is consistent with the action of convection-driven magnetic field emergence and reconnection: the magnetic carpet (Schrijver et al. 1997, 1998; Priest & Schrijver 1999; Priest et al. 2002; Priest & Forbes 2000; Wang 1998).

We have demonstrated that the driven reconnection events largely neighbor the supergranular boundaries and propose that they contain plasma that is loaded and driven by the magnetic carpet's relentless stirring and destruction of the injected and advected magnetic flux (Schrijver & Title 2003). We have deduced that while the net magnetic flux on the scale of a supergranule controls the injection rate of mass and energy into the transition region plasma, it is the global magnetic topology of the plasma that dictates whether the released ejecta provides thermal input to the quiet solar corona or becomes a tributary to the solar wind.

The magnetoconvection-driven reconnection and resulting ejecta that we observe and have discussed has significant impact on the energetics of the outer solar atmosphere. The same must be true for stellar atmospheres for which dynamo-driven, cyclic magnetic field behavior has been observed in their optical/UV/EUV radiative output. The hypothesis presented in this paper can be directly tested by the instruments on the upcoming *Hinode* (formerly *Solar-B*) satellite and should provide motivating science for the *Solar Probe* and *Solar Orbiter* missions currently in the preproposal phase.

We would like to thank David Alexander, Tom Bogdan, Robin Canup, Joe Gurman, Stuart Jefferies, Philip Judge, Bob Leamon, Nathan Schwadron, Meredith Wills-Davey, and several anonymous referees for kind assistance, helpful discussions, and

[3] Similarly, anomalous changes in other chromospheric line widths observed when crossing from quiet-Sun to plage regions (regions of net-zero mean field flux to ones with very large polarity imbalance) that have been largely attributed to changes in the "microturbulence" (Simon et al. 1980), might be considered simply as the natural interface between a thermal (quiet Sun; mean zero field) and a nonthermal (plage; closed topology but large nonzero mean field) process. The work of Worrall & Wilson (1972, 1973), van Breda et al. (1995), and Worrall (2002) on other chromospheric spectral abnormalities may be considered with the same perspective.

comments on the manuscript that have greatly influenced the ideas presented. This material is based on work carried out at the Southwest Research Institute that is supported in part by the National Aeronautics and Space Administration under grants issued under the Living with a Star, Sun-Earth Connection Guest Investigator Programs and Solar Data Analysis Center, specifically grants NAG5-13450 and NAG5-11594 (to D. M. H.) in the early and NNG05GM75G, NNG06GC89G, NNG05GQ70G (to S. W. M.) in the closing phase of the work reported. The SUMER project is financially supported by DLR, CNES, NASA, and the ESA PRODEX Program (Swiss contribution). SUMER is part of *SOHO*, the *Solar and Heliospheric Observatory*, of ESA and NASA. This paper is dedicated to the memory of Alan Stuart McIntosh (1988–1994).

REFERENCES

Aiouaz, T., Peter, H., & Lemaire, P. 2005, A&A, 435, 713
Aiouaz, T., & Rast, M. P. 2006, ApJ, 647, L183
Alissandrakis, C. E. 1981, A&A, 100, 197
Athay, R. G., & Thomas, R. N. 1961, Physics of the Solar Chromopshere (New York: Interscience)
Athay, R. G., et al. 1980, Sol. Phys., 66, 357
Beckers, J. M. 1968, Sol. Phys., 3, 367
Berger, T. E., & Title, A. M. 2001, ApJ, 553, 449
Bewsher, D., et al. 2005, A&A, 432, 307
Bray, R. J. 1973, Sol. Phys., 29, 317
Bray, R. J., & Loughhead, R. E. 1973, The Solar Chromosphere (London: Chapman and Hall)
Bruner, E. C., & Lites, B. W. 1979, ApJ, 228, 322
Cattaneo, F., Emonet, T., & Weiss, N. 2003, ApJ, 588, 1183
Czaykowska, A., et al. 1999, ApJ, 521, L75
Dammasch, I. E., et al. 1999, A&A, 346, 285
Davey, A. R., McIntosh, S. W., & Hassler, D. M. 2006, ApJS, in press
Delaboudiniére, J.-P., et al. 1995, Sol. Phys., 162, 291
De Pontieu, B., Erdelyi, R., & James, S. P. 2004, Nature, 430, 536
Dere, K. P., et al. 1989, ApJ, 345, L95
Dupree, A. K., Penn, M. J., & Jones, H. P. 1996, ApJ, 467, L121
Fawcett, B. C., Jones, B. B., & Wilson, R. 1961, Proc. Phys. Soc. 78, 1223
Feldman, U., & Laming, J. M. 2000, Phys. Scr., 61, 222
Fleck, B., Domingo, V., & Poland, A. I. 1995, The *SOHO* Mission (Dordrecht: Kluwer)
Foukal, P. V. 1976, ApJ, 210, 575
———. 1977, ApJ, 218, 539
Gary, G. A. 1989, ApJS, 69, 323
Gebbie, K. B., et al. 1981, ApJ, 251, L115
Geiss, J., et al. 1995, Science, 268, 1033
Hansteen, V. 1993, ApJ, 402, 741
Hansteen, V., Maltby, P., & Malagoli, A. 1996, in ASP Conf. Ser. 111, Magnetic Reconnection in the Solar Atmosphere, R. D. Bentley & J. T. Mariska (San Francisco: ASP), 116
Hagenaar, H. J., Schrijver, C. J., & Title, A. M. 1997, ApJ, 481, 988
Hagenaar, H. J., et al. 1999, ApJ, 511, 932
Hassler, D. M., et al. 1999, Science, 283, 810
Harrison, R. A. 1997, Sol. Phys., 175, 467
Innes, D. E., et al. 1997, Nature, 386, 811
Ionson, J. A. 1978, ApJ, 226, 650
Jefferies, S. M., et al. 2006, ApJ, submitted
Ko, Y.-K., et al. 2006, ApJ, 646, 1275
Laming, J. M. 2004, ApJ, 614, 1063
Leamon, R. J., & McIntosh, S. W. 2006, ApJL, submitted
Lin, G., et al. 2003, Cytometry, 56A, 23
———. 2005, Cytometry, 63A, 20
Lites, B. W. 2001, ApJ, 573, 431
Madjarska, M. S., et al. 2006, A&A, 452, L11
Mazzotta, P., Mazzitelli, G., Colafrancesco, S., & Vittorio, N. 1998, A&AS, 133, 403
McComas, D. J., et al. 1998, Geophys. Res. Lett., 25, 1
———. 2000, J. Geophys. Res., 105, 10419
McIntosh, S. W. 2006, ApJL, submitted
McIntosh, S. W., Davey, A. R., & Hassler, D. M. 2006, ApJ, 644, L87
McIntosh, S. W., & Gurman, J. B. 2005, Sol. Phys., 228, 285
McIntosh, S. W., & Leamon, R. J. 2005, ApJ, 624, L117
Müller, D. A. N., et al. 2005, A&A, 436, 1067
Parker, E. N. 1988, ApJ, 330, 474
———. 1994, Spontaneous Current Sheets in Magnetic Fields: With Applications to Stellar X-Rays (New York: Oxford Univ. Press)
Priest, E. R., & Forbes, T. 2000, Magnetic Reconnection (Cambridge: Cambridge Univ. Press)
Priest, E. R., Heyvaerts, J. F., & Title, A. M. 2002, ApJ, 576, 533
Priest, E. R., & Schrijver, C. J. 1999, Sol. Phys., 190, 1
Raymond, J. C. 1999, Space Sci. Rev., 87, 55
Roberts, W. O. 1945, ApJ, 101, 136
Scherrer, P. H., et al. 1995, Sol. Phys., 162, 129
Schrijver, C. J., & Title, A. M. 2003, ApJ, 597, L165
Schrijver, C. J., et al. 1997, ApJ, 487, 424
———. 1998, Nature, 394, 152
Schwadron, N. A., & McComas, D. J. 2003, ApJ, 599, 1395
Secchi, P. S. 1877, Le Soliel (Paris: Gaultier-Villars)
Simon, G., et al. 1980, A&A, 89, L8
Smith, E. J., et al. 2003, Science, 302, 1165
Sterling, A. C. 2000, Sol. Phys., 196, 79
Title, A. M., & Schrijver, C. J. 1998, in ASP Conf. Ser. 154, The Tenth Cambridge Workshop on Cool Stars, Stellar Systems, and the Sun, ed. R. A. Donahue & J. A. Bookbinder (San Francisco: ASP), 345
Tu, C.-Y., et al. 2005a, Science, 308, 519
———. 2005b, ApJ, 624, L133
van Breda, I. G., Worrall, G., & Foster, D. C. 1995, A&A, 304, 551
Wang, Y.-M. 1998, ApJ, 501, L145
Wang, Y.-M., & Sheeley, N. R. 2004, ApJ, 612, 1196
Warren, H. P., Mariska, J. T., & Wilhelm, K. 1997, ApJ, 490, L187
Wilhelm, K., Dammasch, I. E., & Xia, L. D. 2002, Adv. Space Res., 30, 517
Wilhelm, K., et al. 1995, Sol. Phys., 162, 189
Worrall, G. 2002, MNRAS, 335, 628
Worrall, G., & Wilson, A. M. 1972, Nature, 236, 15
———. 1973, Vistas Astron., 15, 39
Xia, L. D., Marsch, E., & Curdt, W. 2003, A&A, 399, L5
Xia, L. D., Marsch, E., & Wilhelm, K. 2004, A&A, 424, 1025
Yokoyama, T., & Shibata, K. 1998, ApJ, 494, L113
Young, P. R. 2005, A&A, 439, 361